Regulating the pore structure and oxygen vacancies of cobaltosic oxide hollow dodecahedra for an enhanced oxygen evolution reaction

Yao Xiao[1,2], Yibo Wang[1,3], Meiling Xiao[1], Changpeng Liu[1], Shuai Hou[1], Junjie Ge[1] and Wei Xing[1]

Abstract

Engineering an electrocatalytic anode material to boost reaction kinetics is highly desirable for the anodic oxygen evolution reaction (OER), which is the major obstacle for high efficiency water electrolysis. Here, we present a novel kind of Zn-doped Co_3O_4 hollow dodecahedral electrocatalyst. Abundant oxygen vacancy defects are introduced due to the incorporation of Zn^{2+}, which is beneficial for OH^- adsorption and the charge transfer reaction during the OER process. Moreover, the increase in surface area caused by the advanced structure of the hollow porous dodecahedra facilitates mass transport by increasing the surface area. The novel strategy proposed in this study provides an efficient way to design high-performance electrocatalysts for water electrolysis.

Introduction

With an increasing global energy demand and an increasing concern about environmental pollution from fossil fuels, an increasing amount of research on energy conversion from sustainable energy sources has been stimulated[1]. Renewable alternatives such as wind and solar energies are promising future technologies. However, they are intermittent in nature, and the storage of the generated energy is difficult. The electrochemical water splitting technique provides an ideal solution for this issue, where electricity generated from renewable energies can be stored in terms of chemical energy, i.e., in H–H and O–O bonds. The subsequent recombination of hydrogen and oxygen can provide clean and stable electrical energy in an on-demand manner; additionally, the only byproduct is water[2]. However, the efficiency of hydrogen fuel generation from water splitting is severely limited by the sluggish kinetics of oxygen evolution[3]. Therefore, an efficient electrocatalyst for the oxygen evolution reaction (OER) is needed to provide a high current density at a low overpotential and improve the energy conversion efficiency. Although iridium oxide (IrO_2) and ruthenium oxide (RuO_2) are widely recognized as the most active electrocatalysts for the OER[4], their scarcity and high cost have limited their wide application. Therefore, it is urgent to develop cheap and efficient electrocatalysts for the OER process.

Recently, a range of low-cost metal electrocatalysts have been reported to exhibit outstanding catalytic performances for the OER. Among them, transition metal oxides, especially nickel and cobaltosic oxides, have emerged as promising alternates for IrO_2 and RuO_2 because of their abundance, stability and rich variability of valence states[5–9]. The performances of Co_3O_4 catalysts for the OER are generally affected by their morphology and composition. First, it is well known that the performance of catalysts strongly depends on structural parameters, including the particle size, surface area and morphology[10,11]. A series of templates, such as silica[12], carbon[13] and monodispersed polymer[14], can be used to modify the

Correspondence: Shuai Hou (houshuai@ciac.ac.cn) or Junjie Ge (gejj@ciac.ac.cn) or Wei Xing (xingwei@ciac.ac.cn)
[1]State Key Laboratory of Electroanalytical Chemistry, Jilin Province Key Laboratory of Low Carbon Chemical Power, Changchun Institute of Applied Chemistry Chinese Academy of Sciences, 5625 Renmin Street, Changchun 130022, P.R. China
[2]College of Materials Science and Engineering, Qingdao University of Science and Technology, Qingdao 266042, P.R. China
Full list of author information is available at the end of the article
These authors contributed equally: Yao Xiao, Yibo Wang

particle structure of catalysts. However, traditional template-assisted approaches are complicated because they require further postprocessing to remove the templates. Metal organic frameworks (MOFs) can be used as sacrificial templates to overcome the shortcomings mentioned above with an increased surface area and advanced pore structure. For example, Huang's group synthesized highly symmetric Co_3O_4 hollow dodecahedra by a thermal treatment with ZIF-67 as a template[15]. Ohet al. prepared multiball-in-ball hybrid metal oxides with spherical MOFs as sacrificial templates by taking advantage of their unique reactivity and thermal behavior[16]. Second, the catalytic activities of Co_3O_4 for the OER can be improved by doping[17−19]. For instance, a high OER performance has been achieved by using novel hierarchical $Zn_xCo_{3−x}O_4$ nanostructures constructed with small secondary nanoneedles grown on primary rhombus-shaped pillar arrays[17]. Alexander Eychmüller et al. developed a class of nickel cobalt oxide hollow nanosponges that exhibited higher catalytic activity toward the OER compared with its undoped Co_3O_4 counterpart[20]. However, the improved performances of doped Co_3O_4 catalysts are usually ascribed to the increase in the number of active sites caused by the valence state transfer of cobalt, and there is no in-depth and comprehensive elaboration about the effect of doping.

The OER is a liquid-to-gas electrochemical conversion that requires the multiscale control of catalysts to make each involved reaction step proceed smoothly. These steps include sufficient mass transport, abundant active sites and sufficient catalytic capability. Herein, we present a novel Zn-doped Co_3O_4 hollow dodecahedral electrocatalyst with a high catalytic efficiency for the OER using MOFs with different Co/Zn ratios as templates. At the macroscale, its unique porous hollow structure increases catalytic activity by facilitating mass transport and exposing abundant active sites. At the nanoscale, some of the Zn in the precursor was trapped in the lattice of Co_3O_4, replacing both Co^{2+} at tetrahedral sites and Co^{3+} at octahedral sites. Owing to the incorporation of Zn^{2+}, abundant oxygen vacancy defects are introduced. The oxygen vacancies are beneficial for OH^- adsorption[21] and electronic transfers[22], thereby achieving the needed multiscale modulation to synergistically boost the OER electrochemical process.

Experimental section
Synthesis of Zn_xCo-MOF

All chemicals were analytical grade, purchased from Aladdin Chemistry Corporation (Shanghai, China) and used without further purification.

In a typical synthesis[15], $Zn(NO_3)_2 \cdot 6H_2O$ and $Co(NO_3)_2 \cdot 6H_2O$ with different molar ratios of Zn:Co (0, 1:1, 1:3, and 1:5), were mixed in 100 mL of methanol at room temperature. Then, 3.056 g of 2-methylimidazolate was dissolved in another 100 mL of methanol. The above two solutions were then mixed under vigorous stirring at room temperature for 24 h. The precipitates were collected by centrifugation and washed several times with methanol and then dried at 80 °C for 12 h.

Synthesis of the Co_3O_4 hollow dodecahedra

The Co-MOF powder was loaded in a quartz boat and placed in a tube furnace. Then, Co-MOF was heated to 350 °C at a rate of 5 °C min^{-1} and maintained for 30 min in flowing nitrogen. After that, the N_2 was switched to air, and the furnace was maintained at 350 °C for another 30 min in air.

Synthesis of Zn-doped Co_3O_4 hollow dodecahedra

Zn-doped Co_3O_4 hollow dodecahedra were synthesized by the same procedure as 2.2 except that the precursor was Zn_xCo-MOF ($x = 1$:1, 1:3, and 1:5). The Zn-doped Co_3O_4 hollow dodecahedra derived from ZnCo-MOF, $ZnCo_3$-MOF and $ZnCo_5$-MOF were denoted as Zn-doped Co_3O_4-1, Zn-doped Co_3O_4-2, and Zn-doped Co_3O_4-3, respectively.

Materials characterization

X-ray diffraction (XRD) patterns of the catalysts were obtained using a Rigaku-D/MAX-PC2500 X-ray diffractometer (Japan) with Cu Kα (l¼1.5405 Å) as a radiation source and operated at 40 kV and 200 mA. X-ray photoelectron spectroscopy (XPS) was recorded on a Kratos XSAM-800 spectrometer with an Al Kα monochromatic source. Scanning electron microscopy (SEM) images were taken using an FEI XL30 ESEM FEG scanning electron microscope. Transmission electron microscopy (TEM) was carried out with a JEOL2010 microscope operating at 200 kV with a nominal resolution. The porous structure of the samples was investigated using N_2 adsorption at −196 °C using a Micromeritics ASAP 2020 instrument.

Electrochemical measurements

Electrochemical measurements were performed with a Versa STAT potentiostat/galvanostat controlled by Versa Studio software (Princeton Applied Research). A conventional three-electrode cell was used. A Hg/HgO electrode was used as the reference electrode, and Pt foil was used as the counter electrode. Potentials were transferred to a reversible hydrogen electrode (RHE) by adding $(0.098 + 0.059 \text{ pH})$ V. All experiments were carried out at ambient temperature. The working electrode was prepared as follows. The catalyst ink was prepared by dispersing 5 mg of catalyst in 950 mL of ethanol with 50 μL of 5 wt% Nafion solution. Then, 5 μL of the catalyst ink was loaded on a glassy carbon electrode and dried at room

temperature. The mass loading was $0.35 \, mg \, cm^{-2}$. All data are presented with 95% iR compensation.

Results and discussion

Zn-doped Co_3O_4 hollow dodecahedra were prepared by the thermal treatment of MOFs with different Co/Zn ratios. SEM images of the synthesized MOF samples are shown in Fig. S1, in which the formation of highly uniform Co-MOF particles can be clearly observed (Fig. S1A). To further confirm the structure of Co-MOF, a single crystal from different positions of view is shown in the inset of Fig. S1A, revealing its rhombic dodecahedral structure. Figure S1B exhibits the SEM image of $ZnCo_3$-MOF. $ZnCo_3$-MOF retains its dodecahedral crystal structure despite different contents of Zn doping. Figure 1A presents the SEM image of Co_3O_4 hollow dodecahedra derived from the thermal treatment of Co-MOF, demonstrating that the dodecahedral morphology of the Co-MOF precursor is well preserved. The rough surface of the dodecahedra indicates the polycrystalline nature of the Co-MOF, with the formation of connected nanoparticles due to the confinement of the MOF. An evident porous structure is noticed due to the removal of carbon during the thermal treatment process. Zn-doped Co_3O_4-2 almost preserves the dodecahedral structure except for a slight collapse, as shown in Fig. 1B. The crystal structure of Zn-doped Co_3O_4-2 can be further confirmed by TEM. As displayed in Fig. 1C, the inner part of the dodecahedra is brighter than the outer part, confirming the hollow nanostructure of the Co_3O_4-2 particles. The high-resolution TEM (HRTEM) image taken of Zn-doped Co_3O_4-2 (Fig. 1D) reveals clear lattice fringes with interplanar spacings of 0.24 and 0.28 nm corresponding to the (311) and (220) planes of Co_3O_4, respectively. The selective area electron diffraction (SAED) pattern (Fig. 1E) shows several bright rings consisting of discrete spots, which can be indexed to the (220), (311), and (400) planes of Co_3O_4. Figure 1F demonstrates the scanning TEM (STEM) image and the corresponding EDX elemental mapping images of Co, Zn, and O of Zn-doped Co_3O_4-2, revealing that Co, Zn, and O are uniformly distributed. The X-ray diffraction (XRD) patterns of different samples are presented in Fig. 2A. According to the standard JCPD card No. 43-1003, the diffraction peaks emerging at 19.0, 31.3, 36.8, 59.4, and 65.2° are related to the (111), (220), (311), (511), and (440) planes of cubic-phase Co_3O_4. For the doped samples, no additional diffraction peaks appear regardless of the variation in the Co/Zn ratio, which indicates the isomorphous replacement of Zn^{2+} in the Co_3O_4 lattice[23]. It is noted that broadening in the diffraction peaks is observed with an increased Zn content in the oxides, which is ascribable to the decrease in particle size of the Zn-doped Co_3O_4 samples[24].

X-ray photoelectron spectroscopy (XPS) was performed to quantify O, Co, and Zn in the samples, as well as to investigate their chemical states and stoichiometry. The XPS survey spectra of Zn-doped Co_3O_4 catalysts confirm the presence of Zn (Fig. S2). As presented in Fig. S3, two major peaks centered at 1044.2 and 1021.0 eV can be attributed to Zn 2p3/2 and 2p1/2 of Zn^{2+}, respectively[25], indicating that Zn is successfully doped into the Co_3O_4 hollow dodecahedra. The detailed chemical states of the Co and O of the Co_3O_4 dodecahedra and Zn-doped Co_3O_4-2 are illustrated in Fig. 2B, C. Figure 2B presents the high-resolution Co 2p spectra, in which the peaks located at 779.5 and 794.5 eV are assigned to the position of Co^{3+} and the rest of the peaks are assigned to Co^{2+}. The percentage of Co^{3+} can be determined by integrating the peaks of Co^{3+} [26], which are 75.8%, 71.5%, 69.4%, and 72.3% for the Co_3O_4 dodecahedra, Zn-doped Co_3O_4-3, Zn-doped Co_3O_4-2 and Zn-doped Co_3O_4-1, respectively (Fig. 2B and Table S1). Moreover, the number of surface oxygen vacancies increases due to Zn^{2+} doping, which can be confirmed by the O 1 s XPS spectra (Fig. 2C). The O1s XPS spectrum can be deconvoluted into several peaks, where the peak at ~532 eV indicates the presence of surface oxygen vacancies for Co_3O_4[27,28]. Remarkably, when the concentration of Zn^{2+} is increased, the percentage of oxygen vacancies reaches 34.3% for Zn-doped Co_3O_4-2 and then decreases with further increases in the doping amount of Zn (Fig. 2C and Table S2). To further verify the differences in the oxygen vacancy concentrations, the electron paramagnetic resonance (EPR) spectra of different samples were investigated. The fingerprint signal at $g = 2.003$ appears in the spectra of EPR, demonstrating the presence of oxygen vacancies[29–31]. As shown in Fig. 2D, the difference in the signal intensity infers the concentration variation of oxygen vacancies, which agrees with the XPS analysis. The highest EPR signal intensity further illustrates that Zn-doped Co_3O_4-2 has the largest oxygen vacancy concentration among the other samples.

The isomorphous replacement of zinc to cobalt occurs easily owing to the similar outermost electronic configuration and ion radius[32]. Specifically, when Co^{2+} is substituted by Zn^{2+}, the coordination of oxygen is independent of the doped atoms. However, it has recently been shown that oxygen vacancies on the surface can be formed by the substitution of Co^{3+} sites by Zn^{2+}[32], due to the conservation of charge. In our case, we observed the same phenomenon, where a low proportion of Co^{3+} is observed with an increase in the number of oxygen vacancies[33,34]. On the basis of these experimental results and the reported literature, a mechanism is proposed, as shown in Fig. 3. With the proper doping amount, Zn^{2+} ions replace Co^{3+} at octahedral sites in the lattice of
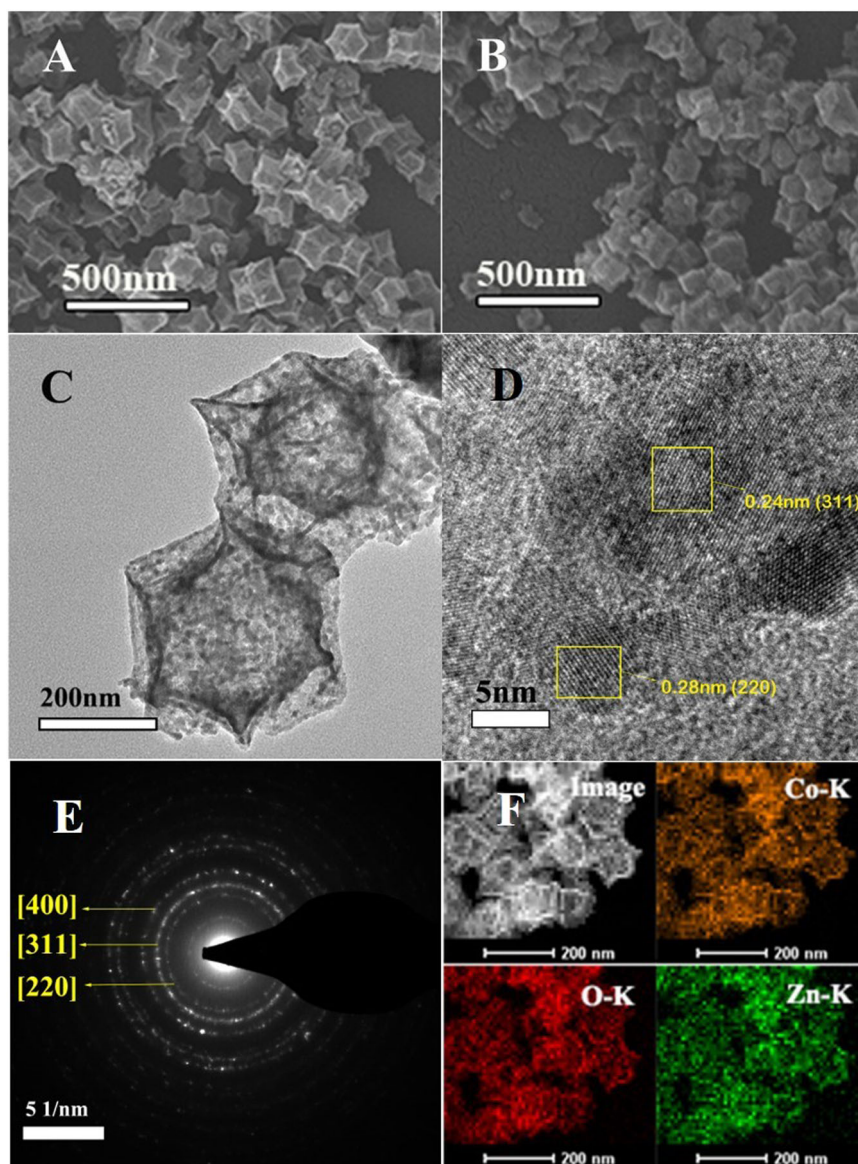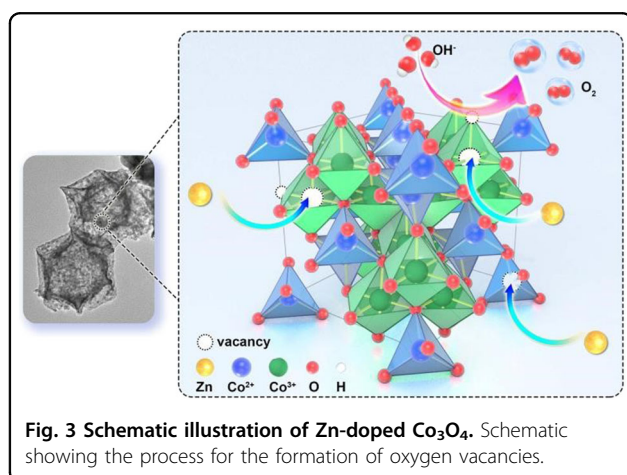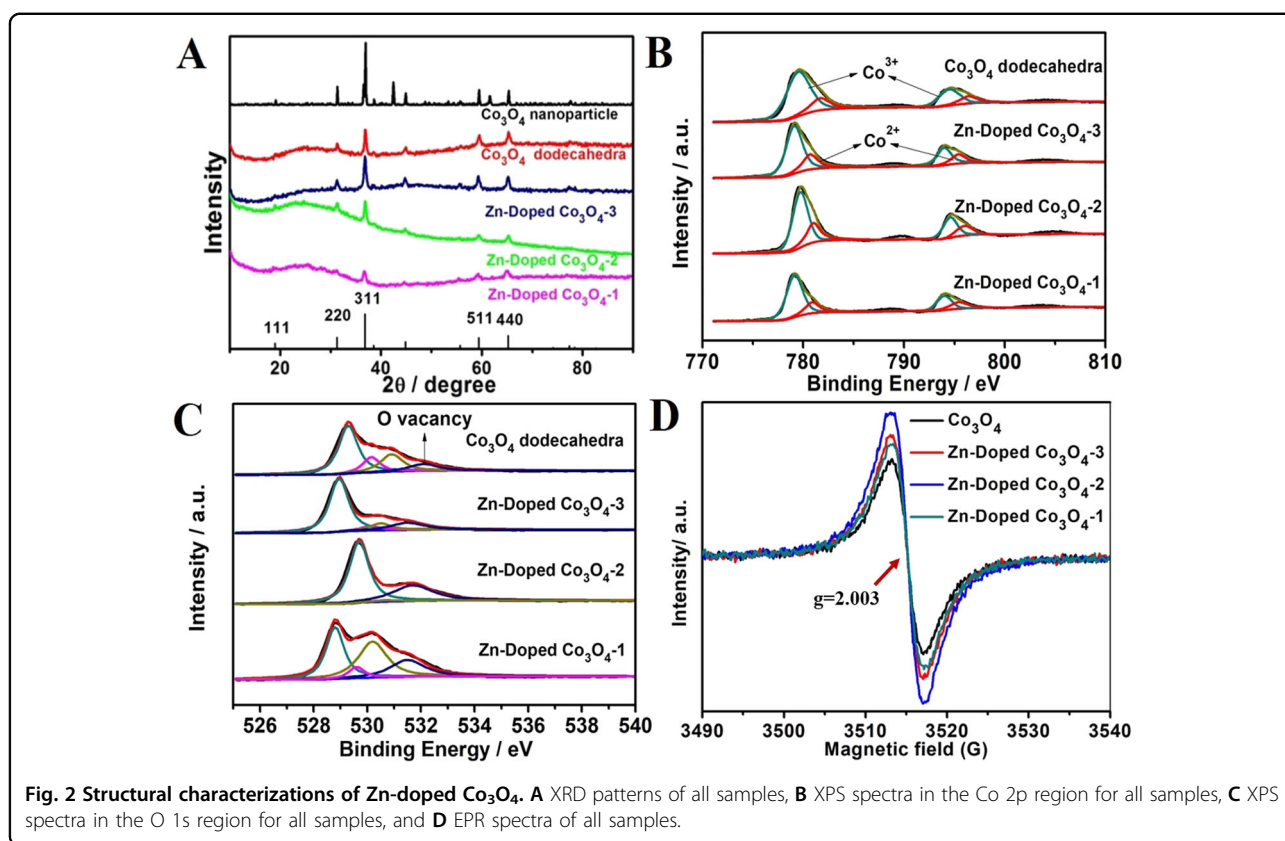
Fig. 1 Morphology characterizations of Zn-doped Co₃O₄. SEM images of **A** Co_3O_4 dodecahedra and **B** Zn-doped Co_3O_4-2, **C** TEM image of Zn-doped Co_3O_4-2, **D** HRTEM image of Zn-doped Co_3O_4-2, **E** SAED pattern of Zn-doped Co_3O_4-2, and **F** STEM image and the corresponding EDX elemental mapping images of Co, Zn, and O for Zn-doped Co_3O_4 hollow dodecahedra.
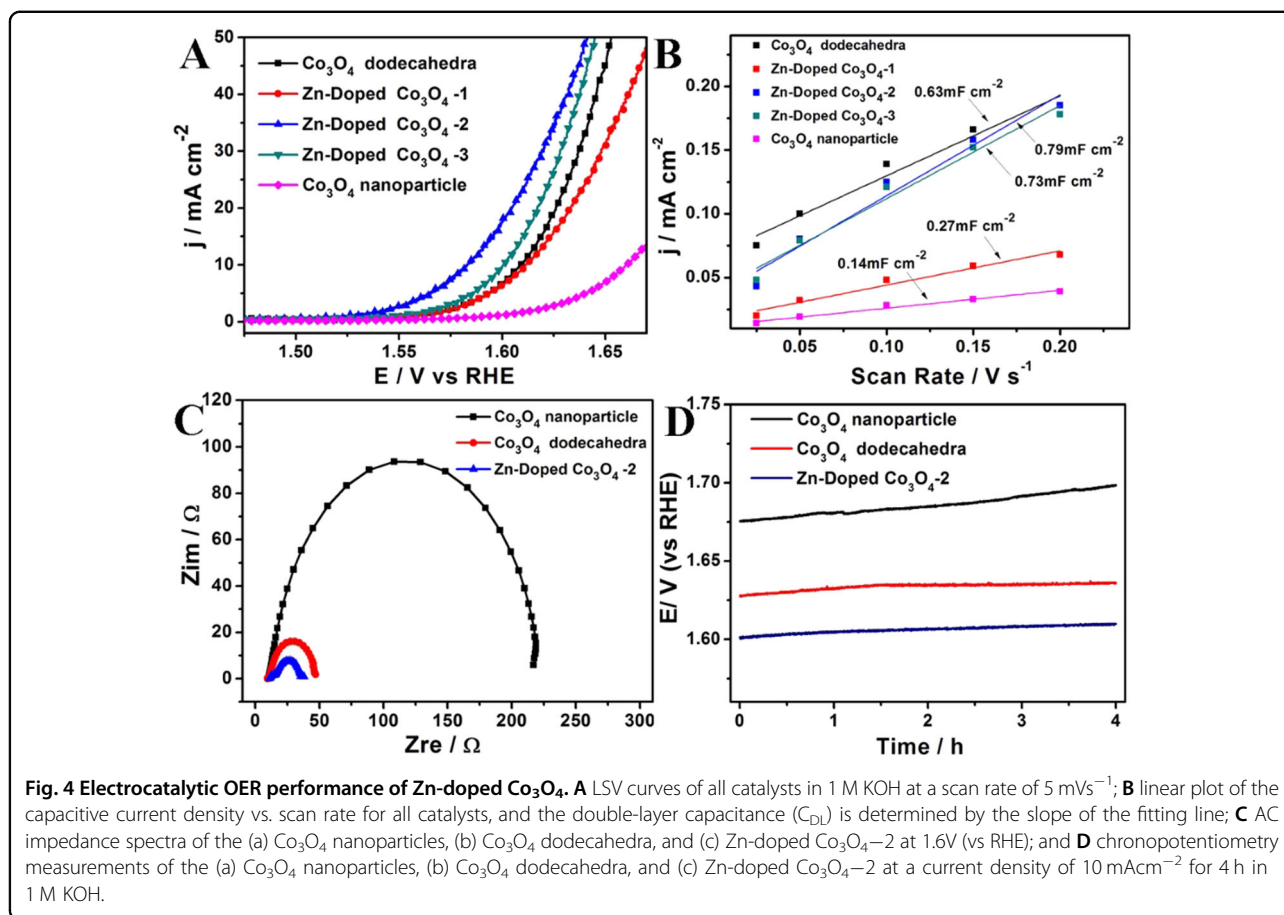
Co_3O_4, which introduces a large number of oxygen vacancies that facilitate OH^- adsorption in a KOH solution during the OER process[21,22]. However, a decrease in the oxygen vacancy concentration is detected for the Zn-doped Co_3O_4-1 sample. We assume the reason for this is that when an excessive amount of the $Zn(NO_3)_2 \cdot 6H_2O$ precursor is added, the probability for the formation of $ZnCo_2O_4$ may increase; the XRD pattern of which is quite similar to that of Co_3O_4[35,36]. As a result, the proportion of Co^{2+} can be decreased, and the corresponding ratio of Co^{3+} may be increased, which can lead to a decrease in the number of oxygen vacancies.

N_2 sorption isotherms are conducted to quantify the porosity and specific surface area of catalysts, and the pore size distribution curve can be obtained by the Barrett–Joyner-Halenda (BJH) method (Fig. S4). Co_3O_4 hollow dodecahedra present a mesoporous structure with a narrow distribution centered at 5 nm (the inset of Fig. S4A). It is notable that with an increasing doping amount of Zn, enlarged mesopores that are above 5 nm are detected (the insets of Fig. S4). Commercial Co_3O_4 particles are also tested for comparison (Fig. S4E). Through the Brunauer-Emmett-Teller (BET) analysis, the surface areas of all catalysts are in the sequence of

Fig. 2 Structural characterizations of Zn-doped Co$_3$O$_4$. A XRD patterns of all samples, **B** XPS spectra in the Co 2p region for all samples, **C** XPS spectra in the O 1s region for all samples, and **D** EPR spectra of all samples.

Fig. 3 Schematic illustration of Zn-doped Co$_3$O$_4$. Schematic showing the process for the formation of oxygen vacancies.

Zn-doped Co$_3$O$_4$-1 (179 m^2/g) > Zn-doped Co$_3$O$_4$-2 (120 m^2/g) > Zn-doped Co$_3$O$_4$-3 (100.1 m^2/g) ≈ Co$_3$O$_4$ hollow dodecahedra (100 m^2/g) > Co$_3$O$_4$ nanoparticles (54 m^2/g). This phenomenon can be attributed to the substitution of Zn ions for Co ions, which results in the decreased crystallinity of cobalt oxide films, as confirmed by the XRD shown in Fig. 2A. As the degree of crystallization decreases, an increase in defects, such as pores, voids, and intragrain boundaries, will emerge, thus causing an increase in the surface area.

The OER performances of all the catalysts were compared in 1 M KOH solution at a scan rate of 5 mV s^{-1} (Fig. 4A). Zn-doped Co$_3$O$_4$-2 shows an overpotential as low as 353 mV at a current density of 10 mA cm^{-2}, which compares favorably to the Co$_3$O$_4$ dodecahedra ($\eta_{10mAcm-2}$ = 379 mV), Co$_3$O$_4$ particles ($\eta_{10mAcm-2}$ = 430 mV) and most of the Co$_3$O$_4$ catalysts in alkaline media (as presented in Table S3). The enhanced activity of Zn-doped Co$_3$O$_4$-2 is derived from its abundant oxygen vacancies. The electrochemical surface areas (ECSAs) of the catalysts can be reflected by the double-layer capacitance (C$_{DL}$). As shown in Fig. S5, the double-layer charging current (j) equals the scan rate (v), and C$_{DL}$ is calculated according to the equation j = vC$_{DL}$[37,38]. As shown in Fig. 4B, the catalytic activities for the different catalysts are found to correlate well with the variations in C$_{DL}$ (Zn-doped Co$_3$O$_4$-2 > Zn-doped Co$_3$O$_4$-3 > Co$_3$O$_4$ dodecahedra > Zn-doped Co$_3$O$_4$-1 > Co$_3$O$_4$ nanoparticle). The reason for this result can be ascribed to the enlarged ECSA, which increases accessibility and promotes the reaction[39]. It is worth noting that although Zn-doped Co$_3$O$_4$-1 possesses the largest surface area through BET (179 m^2/g), its ECSA is smaller than that of other Zn-doped Co$_3$O$_4$ samples, probably due to the excessive content of doped Zn. Zn is less catalytically active for the OER; therefore, an excessive content of doped Zn results in a decrease in the number of active sites, thereby leading to poor catalytic

Fig. 4 Electrocatalytic OER performance of Zn-doped Co$_3$O$_4$. A LSV curves of all catalysts in 1 M KOH at a scan rate of 5 mVs^{-1}; **B** linear plot of the capacitive current density vs. scan rate for all catalysts, and the double-layer capacitance (C$_{DL}$) is determined by the slope of the fitting line; **C** AC impedance spectra of the (a) Co$_3$O$_4$ nanoparticles, (b) Co$_3$O$_4$ dodecahedra, and (c) Zn-doped Co$_3$O$_4$−2 at 1.6V (vs RHE); and **D** chronopotentiometry measurements of the (a) Co$_3$O$_4$ nanoparticles, (b) Co$_3$O$_4$ dodecahedra, and (c) Zn-doped Co$_3$O$_4$−2 at a current density of 10 mAcm^{-2} for 4 h in 1 M KOH.

activity. AC impedance spectra are used to probe the charge transfer resistance. It is clear that at 1.6 V, the charge transfer resistances of Zn-doped Co$_3$O$_4$-2 and Co$_3$O$_4$ dodecahedra are much smaller than that of the Co$_3$O$_4$ nanoparticle (Fig. 4C), which demonstrates the facilitation of the OER reaction kinetics and leads to superior electrochemical performance for the OER. Finally, the stability of catalysts is evaluated by using controlled-current electrolysis. The electrodes were held at a constant current density of 10 mA cm^{-2}, while the operating potential was measured as a function of time. As shown in Fig. 4D, during the 4-h electrolysis process, the decay rates for the Co$_3$O$_4$ dodecahedra and Zn-doped Co$_3$O$_4$-2 are 2.25 and 2 mV h^{-1}, respectively, much smaller than the 6 mV h^{-1} for commercial Co$_3$O$_4$ particles. These results show that the hollow dodecahedral structure can improve the catalytic stability of Co$_3$O$_4$ during the electrolysis process.

Conclusion

We prepared Zn-doped Co$_3$O$_4$ hollow dodecahedra with different Co/Zn ratios by the thermal treatment of an MOF, and the resulting products exhibited enhanced electrochemical activity for the OER with a small overpotential of 353 mV at a current density of 10 mA cm^{-2}.

Moreover, an improved OER stability was observed, with a decay rate of 2 mV h^{-1} for the Zn-doped Co$_3$O$_4$ hollow dodecahedra. We believe that the unique architecture (enlarged surface area, porosity) of Zn-doped Co$_3$O$_4$ hollow dodecahedra and the composition change caused by the doping of Zn (increased oxygen defects) are responsible for its superior electrochemical performance. These results emphasize the importance of engineering both the external morphology and internal composition of OER catalysts, where the good interplay between the two leads to greatly boosted electrocatalytic behavior.

Author details
[1]State Key Laboratory of Electroanalytical Chemistry, Jilin Province Key Laboratory of Low Carbon Chemical Power, Changchun Institute of Applied Chemistry Chinese Academy of Sciences, 5625 Renmin Street, Changchun 130022, P.R. China. [2]College of Materials Science and Engineering, Qingdao University of Science and Technology, Qingdao 266042, P.R. China. [3]University of Science and Technology of China, Hefei 230026, P.R. China

References

1. Joya, K. S., Joya, Y. F., Ocakoglu, K. & van de Krol, R. Water-Splitting catalysis and solar fuel devices: artificial leaves on the move. *Angew. Chem. Int. Ed.* **52**, 10426–10437 (2013).
2. Hong, W. T. et al. Toward the rational design of non-precious transition metal oxides for oxygen electrocatalysis. *Energy Environ. Sci.* **8**, 1404–1427 (2015).
3. Suntivich, J., May, K. J., Gasteiger, H. A., Goodenough, J. B. & Shao-Horn, Y. A Perovskite oxide optimized for oxygen evolution catalysis from molecular orbital principles. *Science* **334**, 1383–1385 (2011).
4. Lee, Y., Suntivich, J., May, K. J., Perry, E. E. & Shao-Horn, Y. Synthesis and activities of rutile IrO_2 and RuO_2 nanoparticles for oxygen evolution in acid and alkaline solutions. *J. Phys. Chem. Lett.* **3**, 399–404 (2012).
5. Augustyn, V., Therese, S., Turner, T. C. & Manthiram, A. Nickel-rich layered $LiNi_{1-x}M_xO_2$(M = Mn, Fe, and Co) electrocatalysts with high oxygen evolution reaction activity. *J. Mater. Chem. A* **3**, 16604–16612 (2015).
6. Lambert, T. N. et al. Electrodeposited $Ni_xCo_{3-x}O_4$ nanostructured films as bifunctional oxygen electrocatalysts. *Chem. Commun.* **51**, 9511–9514 (2015).
7. Wang, J. H. et al. Recent progress in cobalt-based heterogeneous catalysts for electrochemical water splitting. *Adv. Mater.* **28**, 215–230 (2016).
8. Han, L., Dong, S. J. & Wang, E. K. Transition-metal (Co, Ni, and Fe)-based electrocatalysts for the water oxidation reaction. *Adv. Mater.* **28**, 9266–9291 (2016).
9. Bae, S. H. et al. Seamlessly conductive 3D nanoarchitecture of core-shell ni-co nanowire network for highly efficient oxygen evolution. *Adv. Energy Mater.* **7**, 1601492 (2017).
10. Zhao, H., Zhu, Y.-P. & Yuan, Z.-Y. Three-dimensional electrocatalysts for sustainable water splitting reactions. *Eur. J. Inorg. Chem.* **2016**, 1916–1923 (2016).
11. Liu, G., Gao, X. S., Wang, K. F., He, D. Y. & Li, J. P. Mesoporous nickel-iron binary oxide nanorods for efficient electrocatalytic water oxidation. *Nano Res.* **10**, 2096–2105 (2017).
12. Ataee-Esfahani, H. et al. Mesoporous metallic cells: design of uniformly sized hollow mesoporous Pt–Ru particles with tunable shell thicknesses. *Small* **9**, 1047–1051 (2013).
13. Wang, B., Chen, J. S., Wu, H. B., Wang, Z. & Lou, X. W. Quasiemulsion-templated formation of α-Fe_2O_3 hollow spheres with enhanced lithium storage properties. *J. Am. Chem. Soc.* **133**, 17146–17148 (2011).
14. Caruso, F., Caruso, R. A. & Mohwald, H. Nanoengineering of inorganic and hybrid hollow spheres by colloidal templating. *Science* **282**, 1111–1114 (1998).
15. Wu, R. et al. Zeolitic imidazolate framework 67-derived high symmetric porous Co_3O_4 hollow dodecahedra with highly enhanced lithium storage capability. *Small* **10**, 1932–1938 (2014).
16. Cho, W., Lee, Y. H., Lee, H. J. & Oh, M. Multi ball-in-ball hybrid metal oxides. *Adv. Mater.* **23**, 1720–1723 (2011).
17. Liu, X. et al. ChemInform Abstract: Hierarchical $Zn_xCo_{3-x}O_4$ nanoarrays with high activity for electrocatalytic oxygen evolution. *Cheminform* **45** (2014).
18. Liu, Z. Q., Cheng, H., Li, N., Ma, T. Y. & Su, Y. Z. $ZnCo_2O_4$ quantum dots anchored on nitrogen-doped carbon nanotubes as reversible oxygen reduction/evolution electrocatalysts. *Adv. Mater.* **28**, 3777–3784 (2016).
19. Menezes, P. W. et al. Cobalt-manganese-based spinels as multifunctional materials that unify catalytic water oxidation and oxygen reduction reactions. *ChemSusChem* **8**, 164–171 (2015).
20. Zhu, C. et al. Nickel cobalt oxide hollow nanosponges as advanced electrocatalysts for the oxygen evolution reaction. *Chem. Commun.* **51**, 7851–7854 (2015).
21. Li, Y., Tan, B. & Wu, Y. Mesoporous Co_3O_4 nanowire arrays for lithium ion batteries with high capacity and rate capability. *Nano Lett.* **8**, 265–270 (2008).
22. Xu, L. et al. Plasma-engraved Co_3O_4 nanosheets with oxygen vacancies and high surface area for the oxygen evolution reaction. *Angew. Chem. Int. Ed.* **55**, 5277–5281 (2016).
23. Chi, B., Li, J., Yang, X., Lin, H. & Wang, N. Electrophoretic deposition of ZnCoO spinel and its electrocatalytic properties for oxygen evolution reaction. *Electrochim. Acta* **50**, 2059–2064 (2005).
24. Shi, N., Cheng, W., Zhou, H., Fan, T. & Niederberger, M. Facile synthesis of monodisperse Co_3O_4 quantum dots with efficient oxygen evolution activity. *Chem. Commun.* **51**, 1338–1340 (2015).
25. Baird, T. et al. Characterisation of cobalt–zinc hydroxycarbonates and their-products of decomposition. *J. Mater. Chem.* **7**, 319–330 (1997).
26. Ma, T. Y., Dai, S., Jaroniec, M. & Qiao, S. Z. Metal-organic framework derived hybrid Co_3O_4-carbon porous nanowire arrays as reversible oxygen evolution electrodes. *J. Am. Chem. Soc.* **136**, 13925–13931 (2014).
27. Tüysüz, H., Liu, Y., Weidenthaler, C. & Schüth, F. Pseudomorphic transformation of highly ordered mesoporous Co_3O_4 to CoO via reduction with glycerol. *J. Am. Chem. Soc.* **130**, 14108–14110 (2008).
28. Liao, L. et al. Efficient solar water-splitting using a nanocrystalline CoO photocatalyst.*Nat. Nanotechnol.* **9**, 69–73 (2014).
29. Zhang, J., Yin, R., Shao, Q., Zhu, T. & Huang, X. Oxygen vacancies in amorphous InOx nanoribbons enhance CO_2 adsorption and activation for CO_2 electroreduction. *Angew. Chem. Int Ed. Engl.* **58**, 5609–5613 (2019).
30. Kim, M. et al. Oxygen-vacancy-introduced $BaSnO_3$-delta photoanodes with tunable band structures for efficient solar-driven water splitting. *Adv. Mater.* **31**, 1903316 (2019).
31. Lei, F. et al. Oxygen vacancies confined in ultrathin indium oxide porous sheets for promoted visible-light water splitting. *J. Am. Chem. Soc.* **136**, 6826–6829 (2014).
32. Liang, G. et al. A long cycle-life high-voltage spinel lithium-ion battery electrode achieved by site-selective doping. *Angew Chem. Int Ed.* **59**, 10594–10602 (2020).
33. Zhuang, L. et al. Ultrathin iron-cobalt oxide nanosheets with abundant oxygen vacancies for the oxygen evolution reaction. *Adv. Mater.* **29**, 1606793 (2017).
34. Xu, Q., Jiang, H., Zhang, H., Jiang, H. & Li, C. Phosphorus-driven mesoporous Co_3O_4 nanosheets with tunable oxygen vacancies for the enhanced oxygen evolution reaction. *Electrochim. Acta* **259**, 962–967 (2018).
35. Wang, Q., Zhu, L., Sun, L., Liu, Y. & Jiao, L. Facile synthesis of hierarchical porous $ZnCo_2O_4$ microspheres for high-performance supercapacitors. *J. Mater. Chem. A* **3**, 982–985 (2015).
36. Wang, S., Ding, Z. & Wang, X. A stable $ZnCo_2O_4$ cocatalyst for photocatalytic CO_2 reduction. *Chem. Commun.* **51**, 1517–1519 (2015).
37. McCrory, C. C. L., Jung, S., Peters, J. C. & Jaramillo, T. F. Benchmarking heterogeneous electrocatalysts for the oxygen evolution reaction. *J. Am. Chem. Soc.* **135**, 16977–16987 (2013).
38. Liu, W., Zhu, M., Liu, J., Li, X. & Liu, J. Flexible asymmetric supercapacitor with high energy density based on optimized MnO_2 cathode and Fe_2O_3 anode. *Chin. Chem. Lett.* **30**, 750–756 (2019).
39. Liu, X. et al. Hierarchical $Zn_xCo_{3-x}O_4$ nanoarrays with high activity for electrocatalytic oxygen evolution. *Chem. Mater.* **26**, 1889–1895 (2014).